

# Phase-change material enabled silicon phase shifter actuated by a highly durable graphene microheater

Shichang Liu<sup>a</sup>, Xing Yang<sup>a</sup>, Liangjun Lu<sup>a,b,c</sup>, Jianping Chen<sup>a,b</sup>, Yu Li<sup>a,b</sup>,  
Guorui Chen<sup>d</sup>, and Linjie Zhou<sup>a,b,\*</sup>

<sup>a</sup>Shanghai Jiao Tong University, Department of Electronic Engineering, Key Laboratory of Advanced Optical Communication Systems and Networks, Shanghai, China

<sup>b</sup>SJTU-Pinghu Institute of Intelligent Optoelectronics, Jiaxing, China

<sup>c</sup>Chinese Academy of Sciences, Shanghai Institute of Microsystem and Information Technology, State Key Laboratory of Materials for Integrated Circuits, Shanghai, China

<sup>d</sup>Shanghai Jiao Tong University, School of Physics and Astronomy, Key Laboratory of Artificial Structures and Quantum Control (Ministry of Education), Shanghai, China

**ABSTRACT.** We demonstrate a high-efficiency silicon optical phase shifter based on a silicon-Sb<sub>2</sub>Se<sub>3</sub> hybrid integrated waveguide. The optical field has large confinement in the Sb<sub>2</sub>Se<sub>3</sub> material, leading to high optical wave modulation efficiency upon phase change of Sb<sub>2</sub>Se<sub>3</sub>. The phase change is initiated by electro-thermal heating generated by a highly durable graphene microheater positioned between the Sb<sub>2</sub>Se<sub>3</sub> strip and the silicon slab of the hybrid waveguide. To effectively couple the phase shifter with single-mode silicon waveguides, we design a two-layer taper structure as a mode spot size converter. Utilizing this phase shifter, we implemented a Mach-Zehnder interferometer structure to function as an optical switch. The number of effective switching events exceeds 30,000, and 66 non-volatile switching levels are obtained. Our work provides an effective solution for introducing highly durable graphene microheaters on silicon-based phase-change platforms.

© The Authors. Published by SPIE under a Creative Commons Attribution 4.0 International License. Distribution or reproduction of this work in whole or in part requires full attribution of the original publication, including its DOI. [DOI: [10.1117/1.JOM.4.3.031207](https://doi.org/10.1117/1.JOM.4.3.031207)]

**Keywords:** integrated photonics; phase-change material; silicon photonics; phase shifter; graphene

Paper 24005SS received Feb. 25, 2024; revised May 23, 2024; accepted May 29, 2024; published Jul. 30, 2024.

## 1 Introduction

Silicon photonics utilizes complementary metal-oxide-semiconductor manufacturing processes to produce integrated photonic devices for optical signal transmission and processing, with a history dating back to the work<sup>1-3</sup> of Soref et al. in the 1980s and 1990s. Tuning in silicon photonic devices is typically achieved by adjusting the refractive index of waveguides, which can be realized through free-carrier plasma dispersion or thermo-optic effects. However, the above two refractive index modulation mechanisms suffer from issues such as long phase shifter length and state volatility, which limit the integration scale of silicon photonics and also result in high power consumption.

Phase-change materials (PCMs) can undergo reversible conversion between amorphous and crystalline states, and their electrical and optical properties exhibit significant contrast between

\*Address all correspondence to Linjie Zhou, [ljzhou@sjtu.edu.cn](mailto:ljzhou@sjtu.edu.cn)

the two states.<sup>4,5</sup> By integrating PCMs on the silicon photonics platform, the size of the device can be effectively reduced, thereby achieving high-density integration.<sup>6–8</sup> Another advantage of PCM is its nonvolatile nature, which does not require any power consumption to maintain the state, thus greatly lowering the power consumption.<sup>9,10</sup> PCMs that are widely used in the field of silicon photonics include  $\text{Ge}_2\text{Sb}_2\text{Te}_5$  (GST),<sup>11–17</sup>  $\text{Ge}_2\text{Sb}_2\text{Se}_4\text{Te}_1$  (GSST),<sup>6,18–23</sup>  $\text{Sb}_2\text{S}_3$ ,<sup>10,24–26</sup> and  $\text{Sb}_2\text{Se}_3$ .<sup>7,27–32</sup> Due to the advantages of PCM, they have been widely used in various applications, including optical switches,<sup>16,17,33</sup> non-volatile memory,<sup>34–36</sup> and optical computing.<sup>13,15,19,37</sup> GST and GSST have high material losses in the crystalline state in the 1550 nm wavelength and are hence mainly used in optical on/off switches.<sup>16,17,33</sup>  $\text{Sb}_2\text{S}_3$  and  $\text{Sb}_2\text{Se}_3$  have low loss characteristics in both states, making them more suitable for pure phase modulation.<sup>7,10</sup>

The phase transition of PCM can be triggered by thermal,<sup>13,14,38</sup> optical,<sup>12,15,39</sup> or electrical<sup>7,11,33</sup> methods, among which the electrical triggering method is highly compatible and scalable with large-scale photonic integrated circuits. For electrical triggering on the silicon platform, the microheater is typically formed by doped silicon<sup>7</sup> or P-I-N diode (PIN) heaters.<sup>11</sup> However, for the silicon nitride platform, other options need to be considered, such as indium tin oxide (ITO)<sup>23</sup> or graphene.<sup>40</sup> Graphene, as a two-dimensional material with excellent electrical and thermal properties, has been introduced into the phase-change photonics platform.<sup>40–43</sup> However, the endurance of graphene microheaters in the previous work is not high, and they experience heater failure issues.<sup>42</sup> This limits the application of graphene microheaters in phase-change photonics.

In this work, we report a novel silicon-PCM hybrid integrated phase shifter by putting a low-loss  $\text{Sb}_2\text{Se}_3$  strip onto a thin silicon slab. This integration enhances the PCM's ability to control the optical field, thereby reducing the length of the phase shifter. A highly durable single-layer graphene (SLG) is utilized as the microheater to stimulate the phase change of  $\text{Sb}_2\text{Se}_3$ . In our design, graphene is transferred onto the flat silicon slab, ensuring high durability during operation. Compared with PIN or doped-silicon microheaters, graphene is not limited to the silicon platform and can be extended to other platforms such as silicon nitride and lithium niobate. The phase shifter is connected to single-mode silicon waveguides through two-layer taper structures. A Mach–Zehnder interferometer (MZI) structure is constructed by incorporating the proposed phase shifters in two arms. The device achieves over 30,000 effective switching events and corresponds to over 15,000 reversible phase-change cycles. A maximum of 66 switching levels is achieved. To the best of our knowledge, this is a silicon-based phase-change photonic device with the highest number of reversal switchings achieved with a graphene microheater. Our work demonstrates the wide-ranging application potential and growth opportunities for graphene microheaters in phase-change photonics.

## 2 Device Design and Simulation

### 2.1 Hybrid Integrated Waveguide

Figure 1 illustrates the schematic structure of our silicon- $\text{Sb}_2\text{Se}_3$  hybrid integrated nonvolatile phase shifter. PCMs are typically deposited on top of silicon waveguides,<sup>7,42</sup> causing the optical beam within the silicon waveguide to interact with the PCM through weak evanescent wave coupling, resulting in a relatively weak interaction. Here, we design a hybrid integrated waveguide that is composed of a thin layer of silicon slab and an  $\text{Sb}_2\text{Se}_3$  strip on top. The lateral optical confinement is enabled by the  $\text{Sb}_2\text{Se}_3$  strip. Optical waveguide mode has a high overlap with the  $\text{Sb}_2\text{Se}_3$ , greatly reducing the length of the phase shifter. Moreover, transferring graphene onto a flat silicon slab is easier compared with a silicon waveguide with sharp corners. The thickness of the silicon slab layer is  $H_{\text{slab}} = 70$  nm. An SLG, possessing high electrical and thermal conductivities, is used as a microheater and placed below  $\text{Sb}_2\text{Se}_3$ . To avoid direct contact between graphene and the underlying silicon slab, resulting in the formation of semiconductor and metal junctions,<sup>42</sup> a 10-nm-thick alumina film ( $H_1 = 10$  nm) separates the graphene from the silicon slab layer. Meanwhile, to prevent potential damage to graphene by subsequent processes and the fracture of graphene caused by volume expansion and contraction<sup>42,44,45</sup> during the phase-change process of  $\text{Sb}_2\text{Se}_3$ , another 10-nm-thick alumina layer ( $H_2 = 10$  nm) is placed between the graphene and the  $\text{Sb}_2\text{Se}_3$  as a protective layer. The cross-section of the  $\text{Sb}_2\text{Se}_3$  strip is  $500$  nm ( $W_{\text{PCM}}$ )  $\times$   $40$  nm ( $H_{\text{PCM}}$ ). Considering the high-temperature phase-change process, to avoid direct contact between  $\text{Sb}_2\text{Se}_3$  and air, a third 60-nm-thick alumina layer is used as a

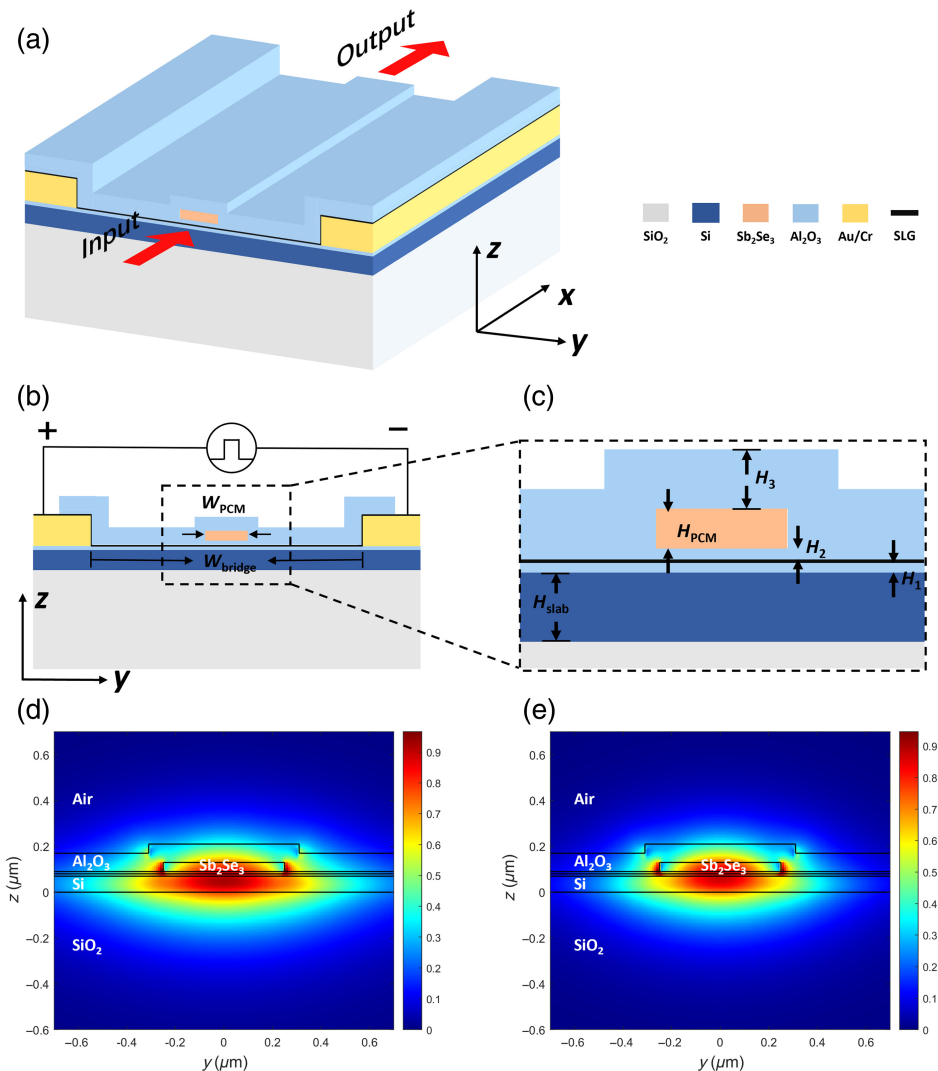


**Fig. 1** Schematic diagram of the proposed silicon-Sb<sub>2</sub>Se<sub>3</sub> hybrid integrated non-volatile phase shifter and TE<sub>0</sub> mode electric-field profiles of the hybrid integrated waveguide in amorphous and crystalline states. (a) Three-dimensional perspective view of the phase shifter. (b) Cross-sectional view of the phase shifter. (c) Enlarged view of the hybrid integrated waveguide. (d) and (e) TE<sub>0</sub> mode electric-field intensity ( $|E|^2$ ) distributions of the hybrid integrated waveguide in (d) the amorphous state and (e) the crystalline state.

protective layer above the Sb<sub>2</sub>Se<sub>3</sub>. This protective layer also effectively prevents the reflow of the Sb<sub>2</sub>Se<sub>3</sub> during the amorphization process. The alumina layer above the graphene in the electrode region is etched away to expose the metal surface for electrical probing, as shown in Fig. 1(b).

To verify that our proposed hybrid integrated waveguide can effectively confine the fundamental mode, we simulated the electric-field distribution of the transverse electric (TE<sub>0</sub>) optical mode. In the simulation, the refractive indices of Sb<sub>2</sub>Se<sub>3</sub> in amorphous and crystalline states were set to  $3.285+0i$  and  $4.050+0i$ ,<sup>46</sup> respectively. Graphene adopts a two-dimensional model based on surface conductivity, which has been supported by Lumerical's optical simulation kit. Figures 1(d) and 1(e) show the TE<sub>0</sub> mode electric-field intensity profiles in the cross-section of the hybrid integrated waveguide in the amorphous and crystalline states, respectively. The electric field is more concentrated in the PCM in the crystalline state compared with the amorphous state due to the higher refractive index of Sb<sub>2</sub>Se<sub>3</sub>. The effective refractive indices of the hybrid integrated waveguide are  $2.021+0.0055i$  in the amorphous state and  $2.144+0.0060i$  in the crystalline state, corresponding to  $\sim 0.19$  and  $\sim 0.21$  dB/ $\mu\text{m}$  propagation losses of the phase shifter, respectively. The corresponding  $\pi$  phase shift length is expressed as

$L_\pi = \lambda / (2(n_{cr} - n_{am}))$ , where  $n_{cr}$  and  $n_{am}$  represent the real part of the effective refractive index of the hybrid integrated waveguide in the amorphous and crystalline states, respectively. Therefore, the  $\pi$  phase shift length at the 1550 nm wavelength is calculated to be  $\sim 6.3 \mu\text{m}$ , which is the shortest phase shifter length based on  $\text{Sb}_2\text{Se}_3$ . The insertion loss in the crystalline state for  $\pi$  phase shift is  $\sim 1.3$  dB, which is mainly caused by the absorption of SLG. In the simulation, when the SLG is removed, then the imaginary part of the effective refractive index becomes 0, which means that the SLG is the main source of the loss.

## 2.2 Mode Converter

To connect the phase shifter to a regular silicon waveguide with low transition loss, it is necessary to design a mode converter to adiabatically tailor the silicon waveguide mode to match that of the hybrid integrated waveguide. Figure 2(a) shows our mode converter based on a two-layer tapered structure. The silicon waveguide has cross-sectional dimensions of 500 nm (width)  $\times$  220 nm (height). In the taper section, the bottom silicon slab thickness is fixed at 70 nm, the same as that in the hybrid waveguide. The slab width ( $W_1$ ) and the ridge width ( $W_2$ ) at the end of the taper are the two design parameters that need to be determined.

We used a three-dimensional finite-difference time-domain simulation to design the mode converter. We performed parameter scans of  $W_1$  and  $W_2$  to obtain the transmissivity and reflectivity of the  $\text{TE}_0$  mode across the interface between the silicon waveguide and the hybrid integrated waveguide. It should be noted that a high similarity of the waveguide mode profiles will result in a high transmission at the interface. The results for amorphous and crystalline states are shown in Figs. 2(b) and 2(c), respectively. Taking into account the simulation results in both amorphous and crystalline states, we chose  $W_1 = 3 \mu\text{m}$  and  $W_2 = 250$  nm to make a good compromise. The coupling loss in both states is less than 0.23 dB. Besides the interface coupling loss, the taper structure itself can also induce certain mode transition loss. We used the eigenmode expansion method to simulate its transmissivity over different lengths. Figure 2(d) shows the simulation results. Considering the fabrication tolerance, we chose a length of  $30 \mu\text{m}$  for the

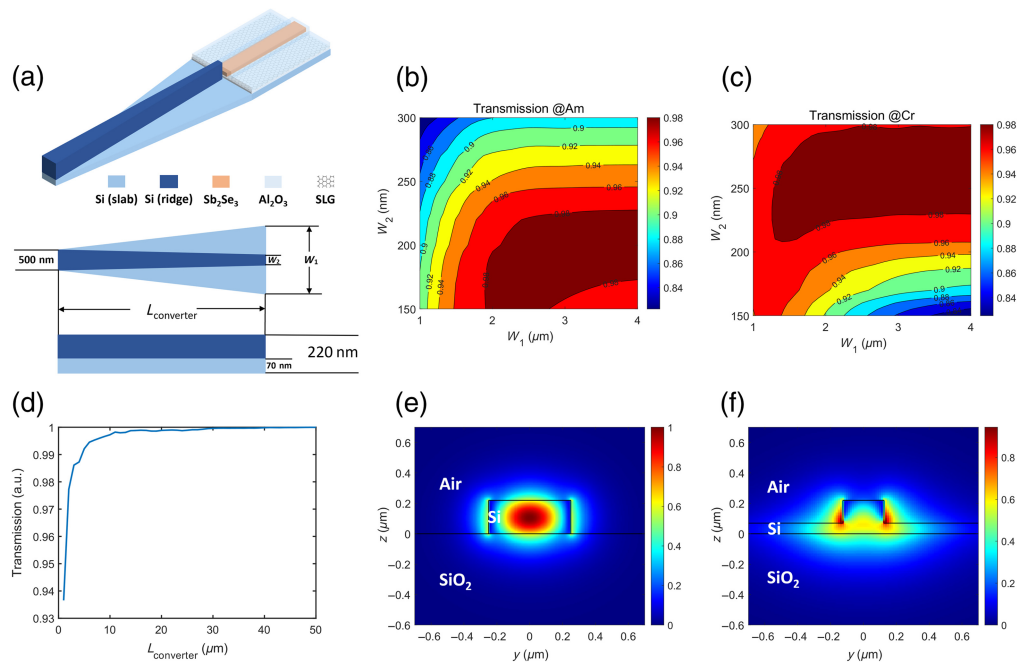


**Fig. 2** Structure and simulation results of the mode converter. (a) Structure of the mode converter consisting of two layers of taper. (b) and (c) Transition loss at the interface of the two types of waveguides in (b) the amorphous (Am) state and (c) the crystalline (Cr) state. (d) Normalized optical transmission through the silicon waveguide taper as a function of taper length. (e) and (f)  $\text{TE}_0$  mode electric-field intensity ( $|E|^2$ ) distributions at (e) the beginning and (f) the end of the mode converter.

mode converter. Figures 2(e) and 2(f) show the waveguide  $TE_0$  modal profiles before and after the mode converter, respectively.

### 2.3 Overall Phase Shifter

We then simulated the overall phase shifter including the active hybrid integrated waveguide in the center and two-mode converters at the two ends, as shown in Fig. 3(a). Considering that an excessively large model size will greatly increase the simulation time, we set the length of the mode converter to  $10\ \mu\text{m}$ . The shorted mode converter only slightly increases the loss according to Fig. 2(d). The length of the phase shifter is set to  $7\ \mu\text{m}$  to cover the  $\pi$  phase shift length.

From the simulated transmission and reflection spectra in Fig. 3(b), the overall insertion loss of the device is less than 2 dB from 1500 to 1600 nm wavelength in both amorphous and crystalline states. The loss mainly comes from the interface coupling loss ( $<0.5\ \text{dB}$ ) and the propagation loss ( $\sim 1.4\ \text{dB}$ ) of the hybrid integrated waveguide. Figures 3(c) and 3(d) illustrate the electric field intensity distributions along two  $x - y$  planes both in the amorphous and crystalline states. Light can go through the phase shifter smoothly with only a weak standing-wave pattern observed at the input waveguide end due to the slight reflection at the interface of the hybrid integrated waveguide.

### 2.4 Graphene Microheater

We simulated the temperature distribution in the phase shifter based on the two-dimensional finite element method. Figure 4 illustrates the temperature responses of two phase-change processes. In the simulation, we only considered the resistance of graphene between the electrodes, without taking into account the contact resistance between the graphene and the metal electrodes, which resulted in a reduction of voltage in the simulation compared with the experiment. The SLG sheet resistance of  $550\ \Omega/\text{sq}^{42}$  was used in the simulation. In the simulation, the left and right boundaries are set to infinite element domains, and the bottom boundary is set to a fixed temperature (293.15 K). For amorphization, we used an electrical pulse with an amplitude of 3.1 V and a width of  $3\ \mu\text{s}$  to heat  $\text{Sb}_2\text{Se}_3$  above its melting temperature ( $T_m = 900\ \text{K}$ ). For

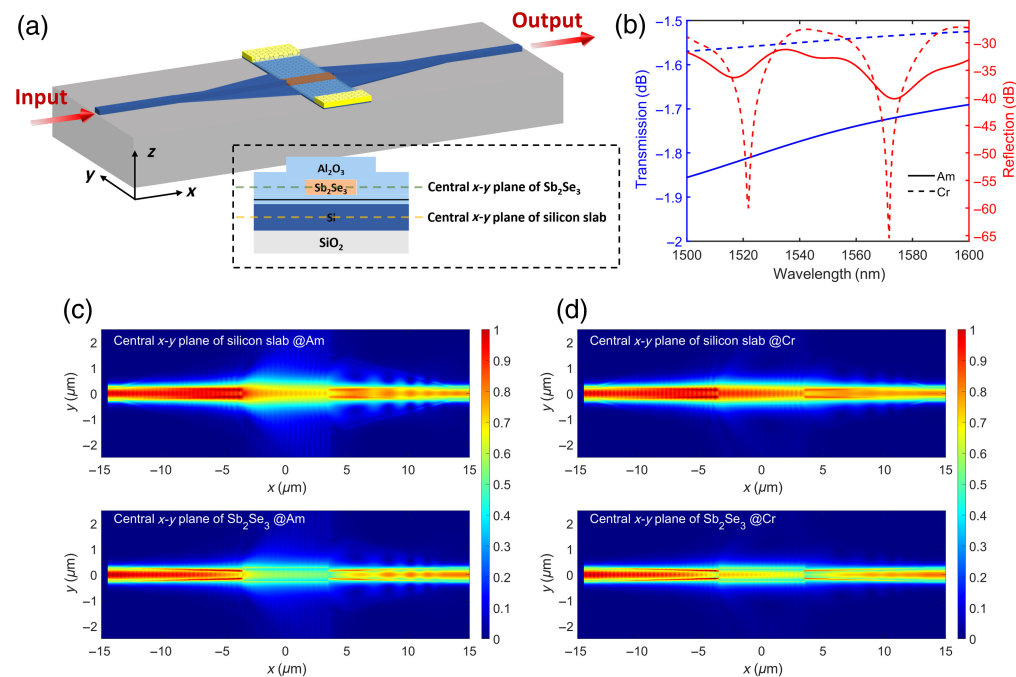


**Fig. 3** Overall phase shifter structure and simulation results. (a) Schematic diagram of the three-dimensional structure of the device. The inset shows the positions of the two  $x-y$  planes in panels (c) and (d). (b) Transmission and reflection spectra in the wavelength range of 1500 to 1600 nm in both amorphous and crystalline states. (c) and (d) Distributions of electric field intensity ( $|E|^2$ ) along the central  $x-y$  plane of the silicon slab layer and the central  $x-y$  plane of the  $\text{Sb}_2\text{Se}_3$  layer along the direction of light propagation in (c) the amorphous state and (d) the crystalline state.

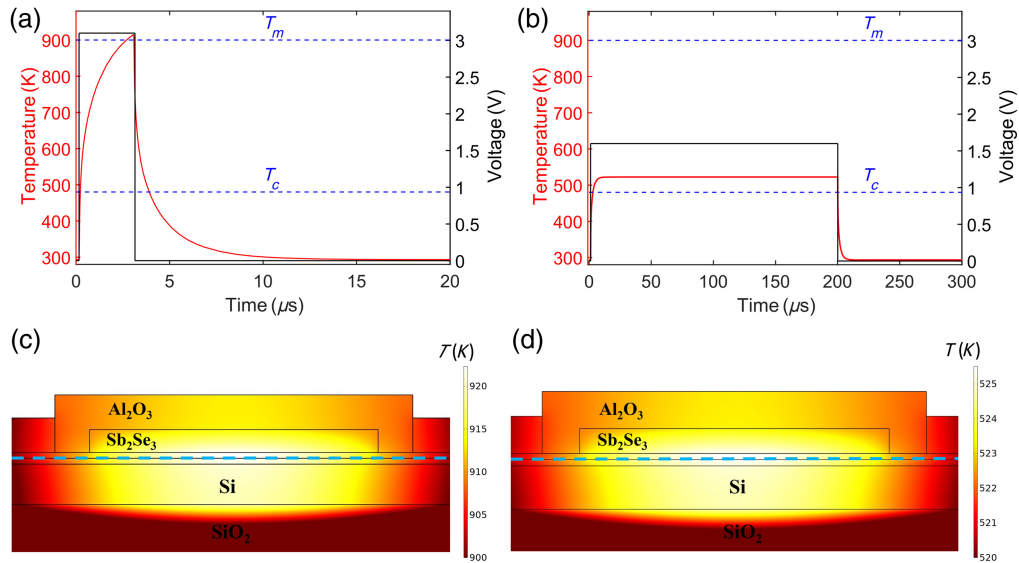


**Fig. 4** Thermal simulation of graphene microheater. (a) and (b) Temperature change in  $\text{Sb}_2\text{Se}_3$  in response to an electrical pulse during (a) the amorphization process and (b) the crystallization process. The probing position is at the minimum temperature point in the  $\text{Sb}_2\text{Se}_3$  region. (c) and (d) Corresponding temperature distributions at the end of (c) the amorphization pulse and (d) the crystallization pulse. The blue dashed line indicates the location of the graphene microheater.

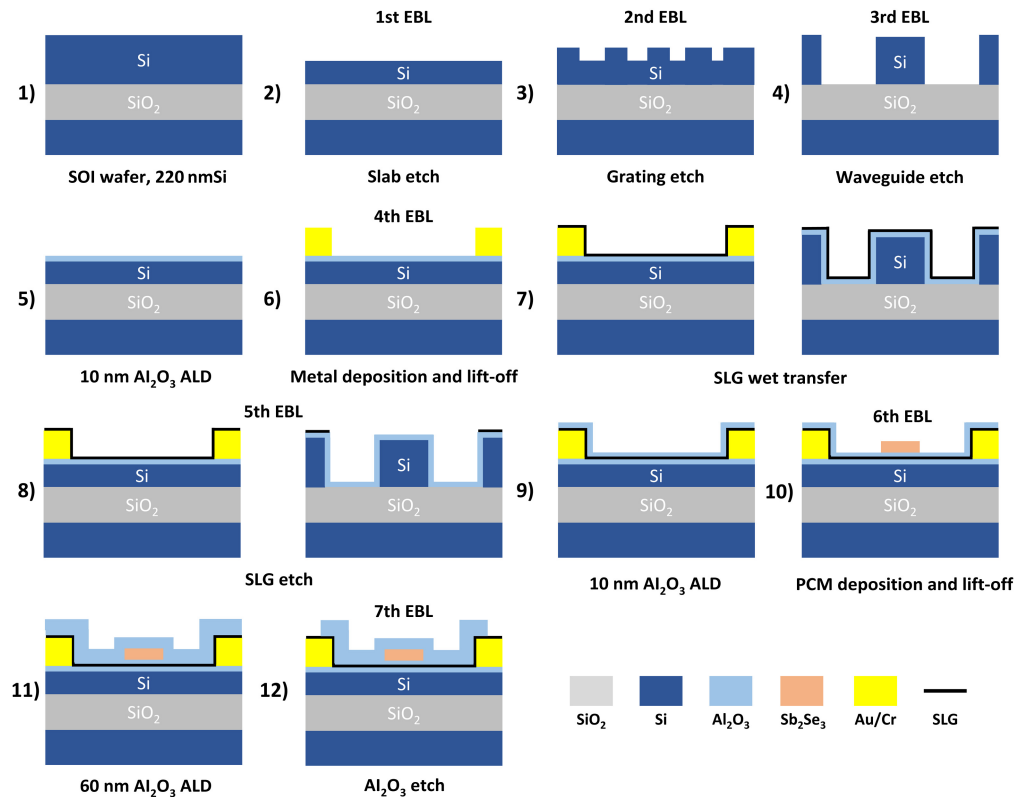


**Fig. 5** Fabrication process flow of the device.

crystallization, we used an electrical pulse with an amplitude of 1.78 V and a width of 200  $\mu\text{s}$  to heat  $\text{Sb}_2\text{Se}_3$  above its crystallization temperature ( $T_c = 480$  K) and below its melting temperature to ensure crystallization. Figures 4(c) and 4(d) illustrate the temperature distributions at the end of the amorphization pulse and the crystallization pulse, respectively. The temperature at the

bottom of  $\text{Sb}_2\text{Se}_3$  is higher than the temperature at the top. Therefore, the material at the bottom will reach the  $T_m$  earlier.

### 3 Device Fabrication

Our devices were fabricated on the silicon-on-insulator (SOI) wafer, which consists of a top silicon layer with a thickness of 220 nm, a buried oxide layer with a thickness of  $2\ \mu\text{m}$ , and a bottom silicon substrate. The device pattern was formed using electron beam lithography (EBL) from the Vistec EBPG5200 system. First, we spin-coated positive resist (CSAR 6200.09) and defined silicon waveguide patterns on the photoresist using EBL. Then, we transferred the developed pattern onto the SOI substrate through inductively coupled plasma (ICP) dry etching. This process requires a total of three EBL-ICP steps, including 70-nm etch depth to form silicon grating, 150-nm etch to form silicon slab, and 220-nm etch to form silicon waveguide. Subsequently, we used atomic layer deposition (ALD) to grow 10-nm-thick alumina on the silicon chip. Thereafter, we spin-coated polymethyl methacrylate (PMMA) and performed EBL to define the metal electrode region. An Au/Cr (120-/10-nm-thick) electrode was grown by electron beam evaporation and patterned using a lift-off process. An SLG film was transferred onto the substrate by the wet method and formed ohmic contact with the underlying Au layer. Only the necessary graphene was retained using EBL and oxygen plasma etching. To protect the graphene film in subsequent processes, we used ALD to grow a 10-nm-thick alumina film as a protective layer. Next, we spin-coated PMMA and performed EBL to open the window for depositing  $\text{Sb}_2\text{Se}_3$ . A 40-nm-thick  $\text{Sb}_2\text{Se}_3$  film was grown by multi-target magnetron sputtering and patterned using the lift-off process. We next grew 60-nm-thick alumina as a protective layer and used EBL and ICP etching to remove the alumina above the electrode to open the probe contact window. The fabrication process flow can be seen in Fig. 5.

Figure 6 shows the optical microscope and scanning electron microscope (SEM) images of the device. From the SEM image, we can see that the etching edge of graphene is visible [as shown by the orange dashed line in Fig. 6(c)] and there is no obvious damage inside, indicating that the graphene film we transferred has high quality and has been well protected in subsequent processes. However, for PCMs [brown area in Fig. 6(c)], we observed an unexpected

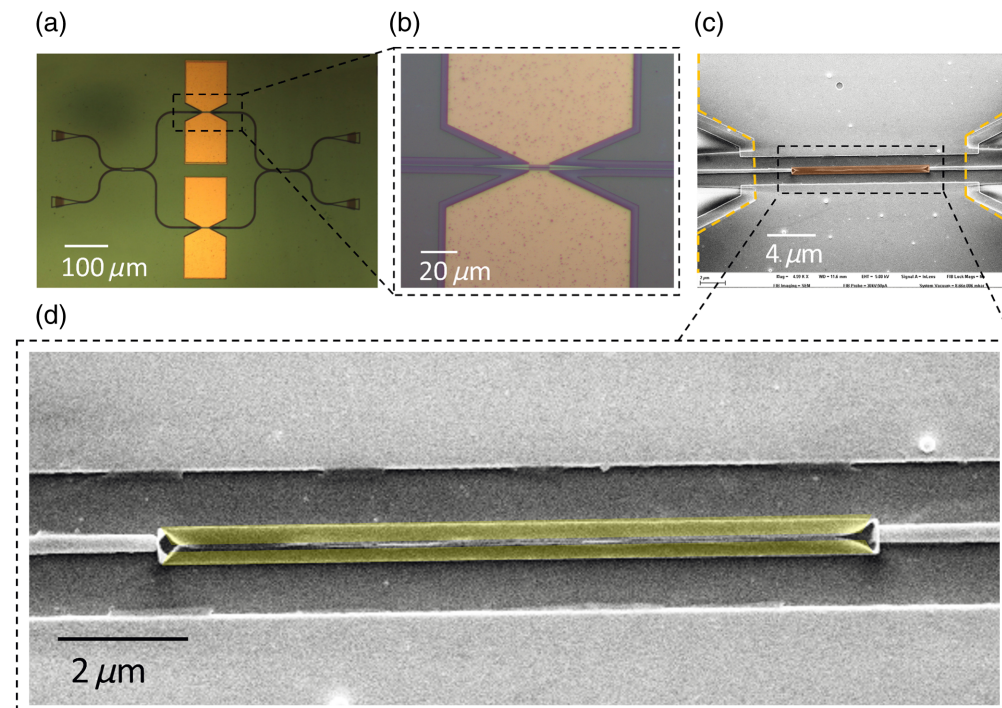


**Fig. 6** Optical microscope and SEM images of the device. (a) Optical microscope image of the device. (b) Enlarged image of the dashed-line enclosed region in panel (a). (c) SEM image of the active waveguide region. (d) Enlarged image of the dashed-line enclosed region in panel (c).

phenomenon where the  $\text{Sb}_2\text{Se}_3$  film folded. In an ideal scenario,  $\text{Sb}_2\text{Se}_3$  should be a single-layer strip. However, we observed clear folding [yellow area in Fig. 6(d)] on both sides. We speculate that it is because, during the lift-off process, the  $\text{Sb}_2\text{Se}_3$  material located on the sidewall of the PMMA did not detach from the substrate. This irregular structure could introduce additional scattering loss.

## 4 Measurement

We used a continuously tunable laser (Agilent 8164B, Santa Clara, California, United States) to measure the optical spectrum in the 1500 to 1580 nm wavelength range. The input polarization was adjusted to TE mode after passing through a polarization controller before it was vertically coupled into the waveguide through a grating coupler. The coupling loss is  $\sim 4$  to 5 dB/facet. The output light from the device was detected by an optical power detector (Agilent 81636B). The electrical pulses used for inducing phase change were generated by an arbitrary waveform generator (AWG, Agilent 81150A) and applied to the electrodes of the device through a pair of metal probes. For each device, we measured its I-V curve (Keysight B2900A, Santa Rosa, California, United States) to obtain the resistance of the graphene microheater and set the load impedance of the AWG to the corresponding value. In this way, the set voltage is the actual voltage loaded onto the device. Before measurement, the chip was thermally annealed at  $200^\circ\text{C}$  for 15 min to initialize  $\text{Sb}_2\text{Se}_3$  into the crystalline state.

We used the designed phase shifter to construct a  $2 \times 2$  MZI, as shown in Fig. 7(a). We first conducted transmission spectrum measurement on routes 2 to 4 of the device, where light is input from port 2 and output from port 4, as shown by the blue curve in Fig. 7(b). To verify that graphene microheaters can effectively induce phase transition, we applied different pulses and monitored the output optical power. Figure 7(c) shows several consecutive measurement results after applying three sets of pulse sequences. The time interval between adjacent pulses is 1 s. The first second of each sequence was measured when no electrical pulse was applied. The first set of pulses [blue curve in Fig. 7(c)] begins at 9 V and increases in a step of 0.2 V, with a fixed pulse width of  $2.3 \mu\text{s}$ . A total of five electrical pulses were applied, with a maximum voltage of 9.8 V. During the application of the first pulse sequence, the output optical power of the device remains decreasing, indicating an increasing amorphization. In the second pulse sequence, the voltage was raised from 9 to 9.8 V with a step of 0.2 V, with its pulse width increased to  $2.6 \mu\text{s}$  to raise the pulse energy. In the first few pulses, we observed an increase rather than a decrease in output

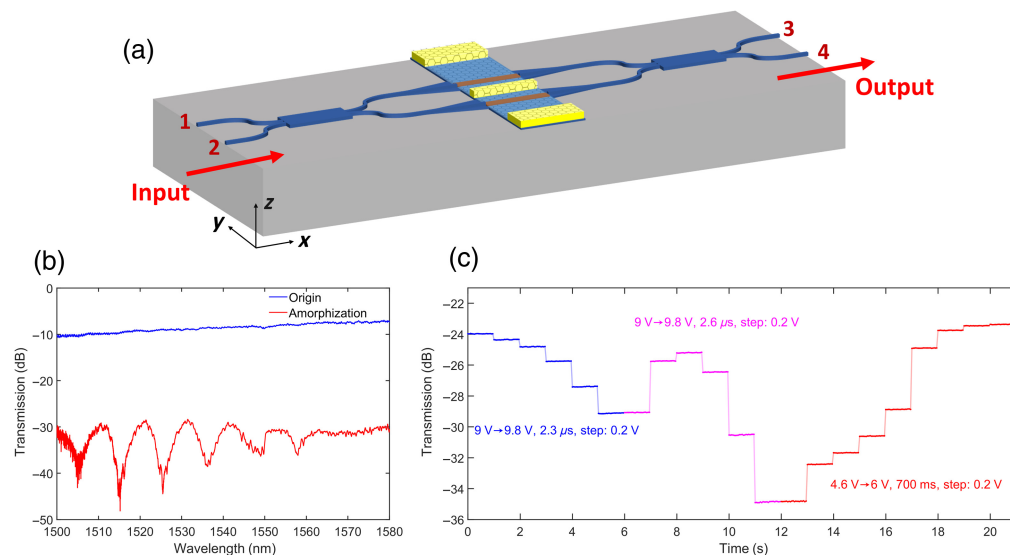


**Fig. 7** Structure and measurement results of MZI based on our proposed phase shifter. (a) MZI structure with the phase shifter integrated on each arm. (b) Transmission spectrum of routes 2 to 4 of the MZI for the original crystalline state and after amorphization of one phase shifter. (c) Variation of output optical power of the MZI when different electrical pulse sequences are applied.

optical power, which means that part of the amorphous  $\text{Sb}_2\text{Se}_3$  had undergone recrystallization. According to the simulation results in Sec. 2.4, we speculate that the energy required for the amorphization of  $\text{Sb}_2\text{Se}_3$  farther away from graphene microheaters should be higher. Therefore, the energy provided by the first few pulses of the second pulse sequence is not sufficient to amorphize the upper part of  $\text{Sb}_2\text{Se}_3$  but rather to recrystallize a portion of  $\text{Sb}_2\text{Se}_3$  that has already been amorphized at the bottom part. When the voltage reaches 9.4 V, the output optical power continues to decrease, indicating that  $\text{Sb}_2\text{Se}_3$  at the upper part also begins to amorphize. For the third set of pulse sequences, we started at 4.6 V and increased with a step of 0.2 V with a fixed pulse width of 700 ms. We applied eight electrical pulses with a maximum voltage of 6 V. On this condition, the output optical power of the device continues to increase, indicating that the  $\text{Sb}_2\text{Se}_3$  has undergone crystallization. During the phase-change process, we measured the transmission spectrum [red curve in Fig. 7(b)] when the output optical power of routes 2 to 4 was at a low level, which corresponds to the case of near-complete amorphization.

Now, PCMs have been widely studied in fields such as optical computing and storage, where multi-level transmission programming is required. Therefore, we also investigated the multi-level operational performance of the device. We first applied a set of amorphization pulse sequences with increasing pulse amplitude and a fixed pulse width of 2.1  $\mu\text{s}$ . The time interval between adjacent pulses is 1 s. The pulse amplitude started from 9.012 V, with a step of 0.012 V, and a total of 65 electrical pulses were applied. A total of 66 non-volatile output levels were achieved, including the initial state. The output optical power of the device changed by  $\sim 14$  dB throughout the entire process. We subsequently investigated the multi-level operation during the crystallization process, as shown in Fig. 8(b). The crystallization process adopts a different pulse sequence from the amorphization process. Here, we fixed the pulse amplitude at 5.2 V and increased the pulse width from 55 to 195 ms in a step of 5 ms, resulting in 30 levels of transmission. It can be seen that in the crystallization process, it is more difficult to achieve multi-level operation compared with the amorphization process, which may be caused by the nucleation stochasticity of the crystallization process.<sup>47</sup> Note that the measurements have undergone a six-point sliding average filtering to reduce the impact of experimental measurement errors.

Another factor that affects the adoption of PCM in integrated photonics applications especially in optical computing and switching is the endurance, which measures the number of times the device can be reconfigured. The endurance of devices is mainly determined by two parts: the PCM and the microheater. Therefore, we also studied the operation up-limit of the device when amorphous and crystalline pulses are applied to continuously change the output optical power between high and low levels. The durability of PCMs is estimated by the variation of extinction ratio (ER), and the endurance of the microheater is estimated by measuring the resistance change of the graphene microheater after applying the pulse sequence. Figure 9 shows the durability test results of the device. We used a short amorphization pulse of 9 V amplitude and 3  $\mu\text{s}$  width and a long crystallization pulse of 4.6 V amplitude and 800 ms width. The time interval is still 1 s. We continuously applied 30,000 electrical pulses on the device, corresponding to 30,000 switching events and 15,000 reversible cycles. Figures 9(b) and 9(c) show the magnified views of the first 50 and the last 50 reversible cycles, respectively. Initially, the ER of the device was at  $\sim 10$  dB, and then, it slowly decreased. After 10,000 reversible cycles, the ER decreased to  $\sim 3$  dB, and the

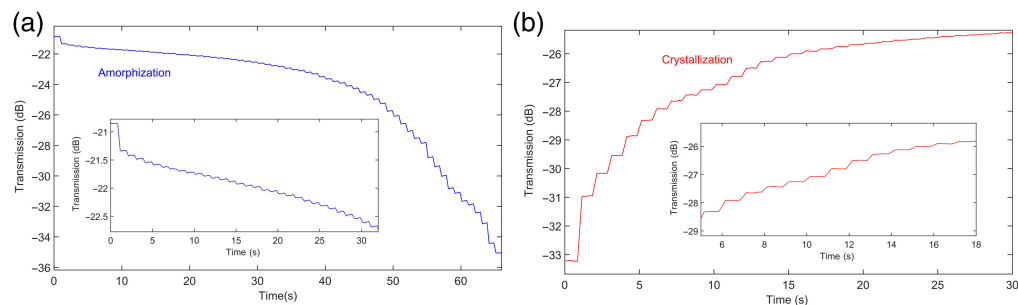


**Fig. 8** Multi-level optical transmission measurement. (a) Amorphization process. The inset shows the measurement for the first 32 levels. (b) Crystallization process. The inset shows the measurement for levels 5 to 18.

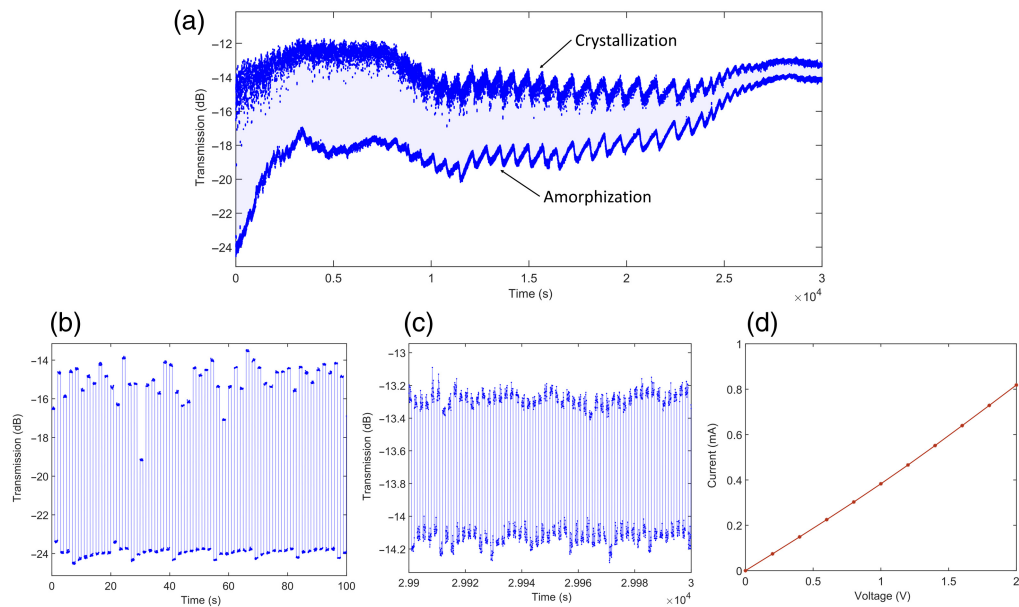


**Fig. 9** Durability test of the device. (a) Change in output optical power of the device under 15,000 reversible cycles. (b) Enlarged view of the first 50 cycles. (c) Enlarged view of the last 50 cycles. (d) I-V curve of the device after 15,000 reversible cycles.

last 50 reversible cycles showed that the ER decreased to  $\sim 1$  dB. The reduction of the ER is attributed to the performance degradation of  $\text{Sb}_2\text{Se}_3$ .<sup>47</sup> After operation for 15,000 reversible cycles, we scanned the I-V curve of the device, as shown in Fig. 9(d). The resistance obtained from the I-V curve is  $\sim 2500 \Omega$ . The contact resistance between graphene and gold is  $\sim 820 \Omega$ ,<sup>42</sup> so the resistance of the graphene film between the electrodes is  $\sim 860 \Omega$ . This demonstrates that our graphene microheater still maintains low resistance after 15,000 reversible cycles, indicating its high durability.

## 5 Discussion

Table 1 summarizes the performance specifications of PCM-based phase-change optical devices. On the SOI platform, on-chip heating can be achieved using doped silicon resistors or PIN

**Table 1** Comparison with other phase-change optical devices.

Ref.	PCM	Heater	ER (dB)	# of levels	# of cycles
11	GST	PIN	10	N/A	2800
10	$\text{Sb}_2\text{S}_3$	PIN	$>10$	32	800
33	GST	PIN	15	2	500
16	GST	Doped Si	10.29	38	N/A
7	$\text{Sb}_2\text{Se}_3$	Doped Si	20	9	125
47	$\text{Sb}_2\text{Se}_3$	PIN	15	64	10,000
48	GSSe	W/Ti	12	16	500,000
17	GST	$\text{In}_2\text{O}_3$	15	64	N/A
41	GSST	Graphene	N/A	4	9
42	GST and $\text{Sb}_2\text{Se}_3$	Graphene	15	14	1000
This work	$\text{Sb}_2\text{Se}_3$	Graphene	10	66	15,000

diodes, while graphene is not limited by the substrate material, thus having a wider range of application prospects. However, some work<sup>41,42</sup> based on graphene microheaters in the early stage showed lower reconfigurability times, which are mainly attributed to the failure of graphene microheaters.<sup>42</sup> Our work has increased the number of operations of the graphene microheater to over 30,000 times, corresponding to more than 15,000 reversible cycles of the device. Our reversible cycle count has increased by an order of magnitude. To our knowledge, this is currently the highest number of reversible cycles achieved on the graphene microheater. In addition, by finely adjusting the amorphous pulses, we have achieved 66 distinguishable non-volatile output levels. This fully demonstrates that our work has further advanced the application of graphene in phase-change photonics, demonstrating excellent performance and enormous potential in terms of device endurance and multi-level operation.

## 6 Conclusions

We have demonstrated a silicon-Sb<sub>2</sub>Se<sub>3</sub> hybrid integrated phase shifter based on high-durability graphene microheaters. The phase shifter is formed by depositing the non-volatile low-loss PCM Sb<sub>2</sub>Se<sub>3</sub> onto the silicon slab layer, with a corresponding  $\pi$  phase shift length of only 6.3  $\mu\text{m}$ . We applied electrical pulses to graphene microheaters using AWG, causing the material to alternate between amorphization and crystallization. By fine-tuning the electrical pulses applied to graphene, we achieved 66 unique non-volatile levels during the amorphization process, with room for additional optimization and enhancement. By applying alternative amorphization and crystallization pulses to the device, the device shows sustained operation for over 15,000 reversible cycles. Noticeably, graphene microheaters are not solely restricted to silicon-based waveguide platforms but also have great potential for application on Si<sub>3</sub>N<sub>4</sub> and lithium niobate waveguides. The work provides an effective method for integrating graphene into phase-change photonics platforms, offering potential applications in fields such as optical computing and storage.

---

### Disclosures

The authors declare no conflicts of interest.

### Code and Data Availability

The code, data, and materials that support the findings of this study are available from the corresponding author upon reasonable request.

### Acknowledgments

This work was supported in part by the National Key R&D Program of China (Grant No. 2021YFB2801300), the National Natural Science Foundation of China (Grant Nos. 62135010, 62090052, 62075128, and 62120106010), the Shanghai Science and Technology Committee Rising-Star Program (Grant No. 23QA1404500), and the Open Research Fund of State Key Laboratory of Materials for Integrated Circuits (Grant No. NKLJC-K2023-06). The authors thank the Center for Advanced Electronic Materials and Devices (AEMD) of Shanghai Jiao Tong University (SJTU) for support in device fabrication.

### References

1. R. Soref and J. Lorenzo, "All-silicon active and passive guided-wave components for  $\lambda = 1.3$  and  $1.6 \mu\text{m}$ ," *IEEE J. Quantum Electron.* **22**(6), 873–879 (1986).
2. M. A. Mentzer et al., "Kramers-Kronig analysis of electro-optical switching in silicon," *Proc. SPIE* **0704**, 32–37 (1987).
3. R. A. Soref, J. Schmidtchen, and K. Petermann, "Large single-mode rib waveguides in GeSi-Si and Si-on-SiO<sub>2</sub>," *IEEE J. Quantum Electron.* **27**(8), 1971–1974 (1991).
4. K. Shportko et al., "Resonant bonding in crystalline phase-change materials," *Nat. Mater.* **7**(8), 653–658 (2008).
5. X. Sun et al., "Realization of multilevel states in phase-change thin films by fast laser pulse irradiation," *Adv. Opt. Mater.* **5**(12), 1700169 (2017).
6. Y. Zhang et al., "Broadband transparent optical phase change materials for high-performance nonvolatile photonics," *Nat. Commun.* **10**(1), 4279 (2019).

7. C. Ríos et al., “Ultra-compact nonvolatile phase shifter based on electrically reprogrammable transparent phase change materials,” *PhotonIX* **3**(1), 26 (2022).
8. J. Zheng et al., “GST-on-silicon hybrid nanophotonic integrated circuits: a non-volatile quasi-continuously reprogrammable platform,” *Opt. Mater. Express* **8**(6), 1551–1561 (2018).
9. Z. Gong et al., “Phase change materials in photonic devices,” *J. Appl. Phys.* **129**(3), 030902 (2021).
10. R. Chen et al., “Non-volatile electrically programmable integrated photonics with a 5-bit operation,” *Nat. Commun.* **14**(1), 3465 (2023).
11. R. Chen et al., “Broadband nonvolatile electrically controlled programmable units in silicon photonics,” *ACS Photonics* **9**(6), 2142–2150 (2022).
12. W. Li et al., “Ultracompact high-extinction-ratio nonvolatile on-chip switches based on structured phase change materials,” *Laser Photonics Rev.* **16**(6), 2100717 (2022).
13. X. Li et al., “Experimental investigation of silicon and silicon nitride platforms for phase-change photonic in-memory computing,” *Optica* **7**(3), 218–225 (2020).
14. Y. Miyatake et al., “Non-volatile compact optical phase shifter based on  $\text{Ge}_2\text{Sb}_2\text{Te}_5$  operating at  $2.3 \mu\text{m}$ ,” *Opt. Mater. Express* **12**(12), 4582–4593 (2022).
15. C. Ríos et al., “In-memory computing on a photonic platform,” *Sci. Adv.* **5**(2), eaau5759 (2019).
16. D. Wu et al., “Resonant multilevel optical switching with phase change material GST,” *Nanophotonics* **11**(15), 3437–3446 (2022).
17. C. Zhang et al., “Nonvolatile multilevel switching of silicon photonic devices with  $\text{In}_2\text{O}_3/\text{GST}$  segmented structures,” *Adv. Opt. Mater.* **11**(8), 2202748 (2023).
18. W. Li, C. Qiu, and A. Wu, “Nonvolatile reconfigurable phase-shifted Bragg grating filter with tunable wavelength and extinction ratio,” *IEEE Photonics J.* **15**(3), 1–7 (2023).
19. R. R. Ghosh and A. Dhawan, “Low loss, broadband, and non-volatile ‘directed logic operations’ using phase change materials in silicon photonics,” *IEEE J. Quantum Electron.* **59**(3), 1–13 (2023).
20. J. He et al., “Design of a multi-functional integrated optical switch based on phase change materials,” *Photonics* **9**(5), 320 (2022).
21. S. Mohammadi-Pouyan, M. Afrouzmehr, and D. Abbott, “Ultra compact bend-less Mach-Zehnder modulator based on GSST phase change material,” *Opt. Mater. Express* **12**(8), 2982–2994 (2022).
22. T. Liu et al., “ $\text{Ge}_2\text{Sb}_2\text{Se}_4\text{Te}_1$ -assisted non-volatile silicon mode selective switch,” *Opt. Mater. Express* **12**(7), 2584–2593 (2022).
23. F. De Leonardis et al., “Broadband electro-optical crossbar switches using low-loss  $\text{Ge}_2\text{Sb}_2\text{Se}_4\text{Te}_1$  phase change material,” *J. Lightwave Technol.* **37**(13), 3183–3191 (2019).
24. H. Chen et al., “Ultra-compact  $\text{Sb}_2\text{S}_3$ -silicon hybrid integrated arbitrarily cascaded tunable mode converter,” *IEEE Photonics J.* **14**(2), 1–7 (2022).
25. C. Song et al., “Compact nonvolatile  $2 \times 2$  photonic switch based on two-mode interference,” *Opt. Express* **30**(17), 30430–30440 (2022).
26. A. Alquliah et al., “Reconfigurable metasurface-based  $1 \times 2$  waveguide switch,” *Photonics Res.* **9**(10), 2584–2593 (2021).
27. H. Jin et al., “Compact nonvolatile polarization switch using an asymmetric  $\text{Sb}_2\text{Se}_3$ -loaded silicon waveguide,” *Opt. Express* **31**(6), 10684–10693 (2023).
28. K. Lei et al., “Magnetron-sputtered and thermal-evaporated low-loss Sb-Se phase-change films in non-volatile integrated photonics,” *Opt. Mater. Express* **12**(7), 2815–2823 (2022).
29. D. Lawson et al., “Time-resolved reversible optical switching of the ultralow-loss phase change material  $\text{Sb}_2\text{Se}_3$ ,” *J. Opt.* **24**(6), 064013 (2022).
30. Y. Fei et al., “On-chip reconfigurable and ultracompact silicon waveguide mode converters based on nonvolatile optical phase change materials,” *Nanomaterials* **12**(23), 4225 (2022).
31. W. Jia et al., “Reconfigurable and programmable optical devices with phase change materials  $\text{Sb}_2\text{Se}_3$  and  $\text{Sb}_2\text{S}_3$ ,” *Proc. SPIE* **12196**, 1219604 (2022).
32. Y. Su, D. Liu, and M. Zhang, “ $\text{Sb}_2\text{Se}_3$ -assisted reconfigurable broadband Y-junction,” *Opt. Express* **30**(22), 40379–40388 (2022).
33. J. Zheng et al., “Nonvolatile electrically reconfigurable integrated photonic switch enabled by a silicon PIN diode heater,” *Adv. Mater.* **32**(31), 2001218 (2020).
34. C. Gao et al., “Structural optimization of integrated non-volatile photonic memory towards high storage density and low energy consumption,” *Opt. Mater. Express* **12**(7), 2668–2678 (2022).
35. C. Ríos et al., “Integrated all-photonic non-volatile multi-level memory,” *Nat. Photonics* **9**(11), 725–732 (2015).
36. M. Wei et al., “Electrically programmable phase-change photonic memory for optical neural networks with nanoseconds in situ training capability,” *Adv. Photonics* **5**(4), 046004 (2023).
37. X. Li et al., “On-chip phase change optical matrix multiplication core,” in *IEEE Int. Electron Devices Meet. (IEDM)* (2020).

38. P. Xu et al., “Low-loss and broadband nonvolatile phase-change directional coupler switches,” *ACS Photonics* **6**(2), 553–557 (2019).
39. C. Wu et al., “Programmable phase-change metasurfaces on waveguides for multimode photonic convolutional neural network,” *Nat. Commun.* **12**(1), 96 (2021).
40. J. Zheng et al., “Modeling electrical switching of nonvolatile phase-change integrated nanophotonic structures with graphene heaters,” *ACS Appl. Mater. Interfaces* **12**(19), 21827–21836 (2020).
41. C. Ríos et al., “Multi-level electro-thermal switching of optical phase-change materials using graphene,” *Adv. Photonics Res.* **2**(1), 2000034 (2020).
42. Z. Fang et al., “Ultra-low-energy programmable non-volatile silicon photonics based on phase-change materials with graphene heaters,” *Nat. Nanotechnol.* **17**(8), 842–848 (2022).
43. J. Faneca et al., “Graphene microheater for phase change chalcogenides based integrated photonic components [Invited],” *Opt. Mater. Express* **12**(5), 1991–2002 (2022).
44. M. G. Herrmann et al., “Lattice dynamics of  $\text{Sb}_2\text{Se}_3$  from inelastic neutron and x-ray scattering,” *Phys. Status Solidi-b* **257**(6), 2000063 (2020).
45. K. Aryana et al., “Suppressed electronic contribution in thermal conductivity of  $\text{Ge}_2\text{Sb}_2\text{Se}_4\text{Te}$ ,” *Nat. Commun.* **12**(1), 7187 (2021).
46. M. Delaney et al., “A new family of ultralow loss reversible phase-change materials for photonic integrated circuits:  $\text{Sb}_2\text{S}_3$  and  $\text{Sb}_2\text{Se}_3$ ,” *Adv. Funct. Mater.* **30**(36), 2002447 (2020).
47. X. Yang et al., “Non-volatile optical switch element enabled by low-loss phase change material,” *Adv. Funct. Mater.* **33**(42), 2304601 (2023).
48. J. Meng et al., “Electrical programmable multilevel nonvolatile photonic random-access memory,” *Light: Sci. Appl.* **12**(1), 189 (2023).

**Linjie Zhou** received his BS degree in microelectronics from Peking University, Beijing, China, in 2003 and his PhD in electronic and computer engineering from the Hong Kong University of Science and Technology, Hong Kong, in 2007. From 2007 to 2009, he was a postdoctoral researcher at the University of California, Davis, California, United States. In 2010, he joined the State Key Lab of Advanced Optical Communication Systems and Networks, Shanghai Jiao Tong University, Shanghai, China. He is currently a distinguished professor. His research interests include optical devices and photonic integration.

Biographies of the other authors are not available.